Engineering magnetic domain wall energies in $BiFeO_3$ via epitaxial strain: A route to assess skyrmionic stabilities in multiferroics from first principles

Sebastian Meyer [1,2,3,*,†] Bin Xu [4,5,*] Laurent Bellaiche [5] and Bertrand Dupé [1,2,3]

[1]*Nanomat/Q-mat/CESAM, Université de Liège, B-4000 Sart Tilman, Belgium*
[2]*TOM/Q-mat/CESAM, Université de Liège, B-4000 Sart Tilman, Belgium*
[3]*Fonds de la Recherche Scientifique, B-1000 Bruxelles, Belgium*
[4]*Jiangsu Key Laboratory of Frontier Material Physics and Devices, School of Physical Science and Technology, Soochow University, Suzhou 215006, China*
[5]*Smart Ferroic Materials Center, Physics Department and Institute for Nanoscience and Engineering, University of Arkansas, Fayetteville, Arkansas 72701, USA*

(Received 21 November 2023; revised 8 March 2024; accepted 18 April 2024; published 16 May 2024)

Epitaxial strain has emerged as a powerful tool to tune magnetic and ferroelectric properties in functional materials such as in multiferroic perovskite oxides. Here, we use first-principles calculations to explore the evolution of magnetic interactions in the antiferromagnetic (AFM) multiferroic $BiFeO_3$ (BFO), one of the most promising multiferroics for future technology. The epitaxial strain in BFO(001) oriented film is varied between $\varepsilon_{xx,yy} \in [-2\%, +2\%]$. We find that both strengths of the exchange interaction and Dzyaloshinskii-Moriya interaction decrease linearly from compressive to tensile strain whereas the uniaxial magnetocrystalline anisotropy follows a parabolic behavior which lifts the energy degeneracy of the (111) easy plane of bulk BFO. From the trends of the magnetic interactions we can explain the destruction of cycloidal order in compressive strain as observed in experiments due to the increasing anisotropy energy. For tensile strain, we predict that the ground state remains unchanged as a function of strain. By using the domain wall energy, we envision the region where isolated chiral magnetic textures might occur as a function of strain, i.e., where the collinear AFM and the spin spiral energies are equal. This transition between -1.5 and -0.5% of strain should allow topologically stable magnetic states such as antiferromagnetic skyrmions and/or merons to occur. Hence, our paper should trigger experimental and theoretical investigations in this range of strain.

DOI: 10.1103/PhysRevB.109.184431

I. INTRODUCTION

For over a decade, topologically stable magnetic structures, such as domain walls (DWs) and skyrmions, have been studied extensively based on their theoretical prediction in the early 1990's [1,2] and their first experimental observation 20 years later [3,4]. Their potential in low-power high-density information storage, and spintronic applications as well as their unique stability, resistance to external magnetic fields, and efficient dynamics make them a fascinating area of study [5–8]. The formation and control of these skyrmions have primarily been explored in ferromagnetic materials, but their antiferromagnetic counterparts are predicted to exceed their potential [9–12]. While the stabilization of skyrmions in ferromagnets can be achieved, e.g., by the application of external magnetic fields [13–18], antiferromagnets are unaffected by those. Therefore, the stabilization of chiral magnetic textures in antiferromagnets remains a challenge and depends on the precise control of magnetic interactions.

Epitaxial strain allows for precise modification of a material's lattice structure through heteroepitaxial growth and has emerged as a powerful tool to engineer magnetic properties in materials. For example, it offers the means to tailor crystal symmetries [19,20], magnetic anisotropies, and exchange interactions and even to control the magnetic ground state of a material [21]. In this way, skyrmions could be stabilized in ferromagnetic (FM) systems [22–25]. Such a technique can pave the way to the stabilization and control of magnetic structures such as skyrmions in antiferromagnets. Strain engineering has already been used in multiferroic oxides, where several ferroic orders, such as the polarization and the magnetization, can be tuned [26–29]. More interestingly, their coupling, called the magnetoelectric coupling, is affected by strain. Since they do not only possess a magnetoelastic but also a magnetoelectric and piezoelectric coupling, the magnetism can be tuned in various ways. To that end, one of the most promising multiferroic materials is $BiFeO_3$ (BFO) where ferroelectricity and antiferromagnetism can coexist far beyond room temperature [30–34].

Besides being extensively studied in the bulk, the interest in strained BFO has also risen up due to the variety of noncollinear states that it can host. Bulk BFO has an antiferromagnetic (AFM) spin spiral ground state—the so-called type-I cycloid of 62-nm pitch [35,36]. This spin spiral can be destroyed via biaxial strain when BFO thin film is grown on various substrates [21,37–40] or by uniaxial strain [28] which suggests a high magnetoelastic response. This response can affect all magnetic interactions in BFO, e.g., the magnetic

*These authors contributed equally to this work.
†smeyer@uliege.be

exchange, the anisotropy, and the Dzyaloshinskii-Moriya interaction (DMI), the ratios of which have yet to be quantified via density functional theory (DFT). A region of particular importance is the transition between collinear and noncollinear magnetic ground states as a function of strain because more complex isolated magnetic textures, such as skyrmions, antiskyrmions, and merons/antimerons, can form.

In this paper, we explore the different magnetic interactions of $BiFeO_3$ under the influence of biaxial strain based on DFT. Varying the nominal strain $\varepsilon_{xx,yy} \in [-2\%, +2\%]$ from compression to elongation, we determine the magnetic exchange interaction, Dzyaloshinskii-Moriya interaction, and anisotropy energy. We study the influence of epitaxial strain on the magnetism in the Cc phase of BFO to identify the region of strain, where the transition from noncollinear to collinear order takes place. We find that both exchange and DMI decrease linearly with strain whereas the anisotropy follows a parabolic behavior, preferring the $[11\bar{2}]$ direction for compressive strain and the $[1\bar{1}0]$ direction for tensile strain. Following the ratios of magnetic interactions, we conclude that with compressive strain, collinear G-type antiferromagnetic order is enhanced due to an increase of the anisotropy and magnetic exchange over the DMI. In the tensile regime, the results are ambiguous. From our calculations, we expect that the spin spiral ground state of the bulk $R3c$ phase in BFO is preserved; however, since the energies are extremely close, small distortions or impurities can also favor collinear order. At last we analyze the evolution of the domain wall energy to locate the region of strain where chiral noncollinear magnetic textures such as antiferromagnetic skyrmions and/or merons could be stabilized in $BiFeO_3$. We identify the transition between a noncollinear and a collinear ground state in BFO in between -1.5 and -0.5% of compressive strain where such states should occur. The presented paper should therefore trigger experimental and theoretical investigations in that range of strain.

This paper is structured as follows: In Sec. II, we describe our procedure for the DFT calculations. In Sec. III, the results of the DFT calculations are presented, which are discussed in Sec. IV. A conclusive statement is given in Sec. V.

II. METHODS

A. Structural relaxation

We have relaxed all strained structures of $BiFeO_3$ using the ABINIT package [41,42] and the projector augmented wave method [43]. Therefore, strain $\varepsilon = \frac{a' - a_{\mathrm{BFO}}}{a_{\mathrm{BFO}}}$ is applied from -2 to 2% for the in-plane axes of the Cc phase of BFO. Here, a' is the varied in-plane lattice constant and a_{BFO} denotes the BFO bulk lattice constant of the $R3c$ phase. Note that the Cc phase is imposed at $\varepsilon = 0\%$ with the lattice constant of $R3c$ BFO. While ε is varied from compressive strain of -2% to tensile strain of $+2\%$, the other structural parameters are relaxed [indicated by blurred colors of the atoms and bonds; see sketch in Fig. 1(a)].

We have used a $\sqrt{2} \times \sqrt{2} \times 2$ unit cell hosting 20 atoms. The magnetic configuration is chosen as the collinear G-type antiferromagnetic order. We have converged the forces on each atom down to 1×10^{-5} hartree/bohr. The exchange and correlation functional is treated with local spin density approximation $+U$ (LSDA $+ U$), with a Hubbard $U = 4.0$ eV parameter and $J = 0.4$ eV on the Fe atoms, which are typical values for first-principles calculations on BFO [33,44,45]. The wave functions are expanded with a plane-wave basis set using a kinetic energy cutoff of $E_{\mathrm{cut}} = 30$ hartree. By using a k-point mesh for the structural relaxation of $8 \times 8 \times 6$, we obtain a magnetic moment of the Fe atoms of $|m_{\mathrm{Fe}}| = 4.0\,\mu_B$ for all relaxed structures. The results of the relaxation are presented in Figs. 1(b) and 1(c) and are in accordance with previous studies [19,20]. Note that due to the relaxation of all structural

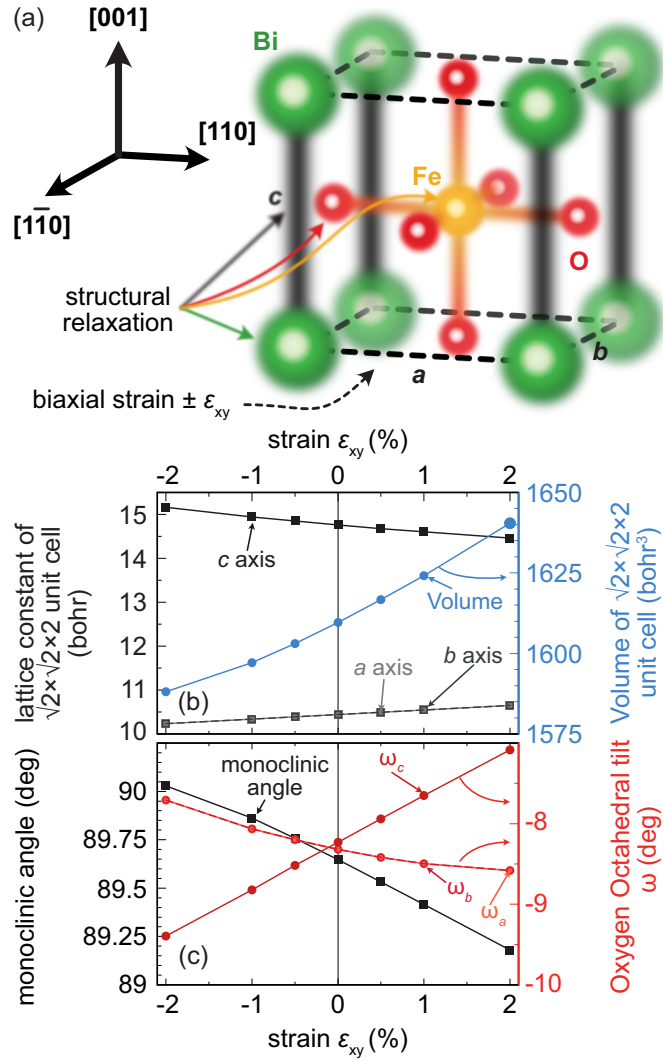

FIG. 1. Structural properties of strained $BiFeO_3$. (a) Sketch of strained Cc BFO in cubic representation: Biaxial strain ε is applied in the xy plane with an angle of 90° between the a and b axis, whereupon the other parameters (c axis, monoclinic angle, and all atomic positions) are relaxed—indicated by blurred colors (for more details, see text). (b) Relaxed lattice constant (a, b, and c axes, squares on left ordinate) vs value of strain. Right ordinate: Unit cell volume (blue filled circles). Note that the relaxation has been done in a $\sqrt{2} \times \sqrt{2} \times 2$ unit cell—the values are presented within this notation. (c) Left ordinate: Monoclinic angle of the c axis (black squares) and components of the oxygen octahedral tilts ω_i around the i axis (red circles for the second ordinate). Note that due to the imposed Cc phase at 0% strain, the tilt angles around the three axes are not exactly on top of each other due to shear strain in the xy plane.

properties, it is not possible to link every single structural contribution to the change of every magnetic interaction separately.

B. Determination of magnetic interactions

We use the relaxed structures as described above to determine the magnetic interactions, such as the Heisenberg exchange interaction, the DMI, and the uniaxial anisotropy energy for each value of strain. The first two interactions are determined by calculating energy dispersions of flat homogeneous spin spiral states without (for the exchange) and with (for the DMI) spin-orbit coupling (SOC). For both interactions, we apply the pseudocubic approximation to compare the results we have obtained for the relaxed $R3c$ structure [45,46].

Spin spirals are the general solution of the Heisenberg model on a periodic lattice and can be characterized by the spin spiral vector $\mathbf{q}$. This vector determines the propagation direction of the spin spiral as well as the canting angle between two neighboring spins. A magnetic moment $\mathbf{M}_i$ at an atom position $\mathbf{r}_i$ is given by

$$\mathbf{M}_i = M(\cos(\mathbf{q}\cdot\mathbf{r}_i), \sin(\mathbf{q}\cdot\mathbf{r}_i), 0) \tag{1}$$

where M is the magnitude of the magnetic moment.

The energy dispersions $E(\mathbf{q})$ are obtained applying the full-potential linearized augmented plane-wave approach [47–49], as implemented in the FLEUR code [50]. For all these calculations, we have used the LSDA+U [51] with a Hubbard $U = 4.0\,\text{eV}$ parameter and $J = 0.4\,\text{eV}$ on the Fe atoms. Muffin-tin radii were set to 2.80, 2.29, and 1.29 bohrs for Bi, Fe, and O atoms, respectively, and a large plane-wave cutoff $k_{\mathbf{max}}$ of 4.6 bohr^{-1}. These parameters result in a magnetic moment of Fe, $M = 4.0\,\mu_\text{B}$ for all phases in agreement with experiments [36]. Calculations along the full paths of the Brillouin zone (BZ) without SOC have been performed self-consistently using the generalized Bloch theorem [52] and a k-point mesh of $10 \times 10 \times 10$. To accurately determine the energies around the magnetic ground state (R points of the BZ) at $|\mathbf{q}| \to R$, the magnetic force theorem [53,54] has been applied using a dense k-point set of 64 000 k points (i.e., $40 \times 40 \times 40$). The energy dispersion without SOC is interpreted using the Heisenberg exchange interaction. For the energy contribution due to SOC, ΔE_SOC, we add SOC in first-order perturbation theory [55,56] for every previously calculated point. The resulting curve has been interpreted with the Dzyaloshinskii-Moriya interaction [57,58].

We determine the Heisenberg exchange interaction constants J_{ij} beyond nearest neighbors by mapping the Heisenberg Hamiltonian

$$\mathcal{H}_\text{ex} = -\sum_{i,j} J_{ij}(\mathbf{m}_i \cdot \mathbf{m}_j) \tag{2}$$

onto the energy dispersion $E(\mathbf{q})$ of flat spin spiral states neglecting SOC where $\mathbf{m}_{i,j} = \mathbf{M}_{i,j}/M_{i,j}$ denotes the renormalized magnetic moment. We include seven neighbors for the exchange interaction using the pseudocubic approximation for all values of strain. To simplify our model, we approximate the curvature of the combined exchange interactions $J_{1,\ldots,7}$ at $\mathbf{q} \to R$, $|\mathbf{q}| \in [R, R-0.1]$ with an effective nearest-neighbor exchange interaction J_eff. J_eff hence describes the same energy dispersion around the ground state as the energy dispersion that is described by $J_{1,\ldots,7}$. More information on this approach can be found in the Appendix and in Refs. [45,46].

For the DMI, we use the calculated data of the energy contribution due to SOC ΔE_SOC. Therefore, we use the converse spin-current (SC) model [46,59,60]

$$\mathcal{H}_\text{SC} = -\sum_{i,j} C_{ij}(\mathbf{u} \times \mathbf{e}_{ij}) \cdot (\mathbf{m}_i \times \mathbf{m}_j) \tag{3}$$

where C_{ij} determines the strength of the DMI, $\mathbf{u}$ is the unit vector along the polarization direction that we fix in the [111] direction, and $\mathbf{e}_{ij}$ is the unit vector between magnetic sites i and j [61]. We include three neighbors for the SC DMI in pseudocubic approximation. For the effective DMI, C_eff, we linearly map Eq. (3) to the SOC contribution at $\mathbf{q} \to R$.

We also have calculated the magnetocrystalline anisotropy energy (MAE) in $BiFeO_3$. For that, we have assumed the collinear G-type AFM states for each structure. The calculations have been done including SOC and a fixed spin quantization axis in the different directions . We have used $20 \times 20 \times 20$ k-point mesh in the whole Brillouin zone and applied the second quantization with the force theorem [53] to determine the energy differences between the hard axis ([111] axis) and other directions as shown in the results. For the description of the domain wall energy, we will use an effective anisotropy K_eff that is the lowest energy of the respective direction with strain.

This method for calculating magnetic interaction in BFO has also been described in detail in Refs. [45,46].

C. Error estimation

In the following, we will analyze small energy differences that qualitatively affect the ground state of $BiFeO_3$. Especially for the DFT calculations, we reach the limit of accuracy below $\approx$0.1 meV. It is impossible to estimate the error in DFT calculations itself stemming mostly from the exchange correlation functional simply because the amount of necessary calculations for that is beyond the scope of any DFT study that is not addressed to that specific problem. Hence, the absolute values in our calculations may vary depending on the functional, and we can only conclude on the trends. The LSDA+U approximation with the functional of Ref. [51] has been used previously in Refs. [45,46].

For the effective magnetic interactions including a fitting procedure in the first step, namely the exchange and the DMI, we will address the error based on the error of the fits. For the DMI, the DFT data at $\mathbf{q} \to R$ is perfectly linear and the value C_eff is determined with a negligible error of less than 0.01%. The values for the exchange interactions J_i on the other hand are fitted with an error ΔJ_i. This error affects our estimate on J_eff because it describes this energy dispersion curve within $\mathbf{q} \to R$. Since the energy is the sum for all J_i, we apply the sum rule to estimate the error on J_eff as

$$\Delta J_\text{eff} = \frac{1}{6}\sqrt{\sum_{i=1}^{7}(\Delta J_i)^2 N_i} \tag{4}$$

where N_i are the number of neighbors in the ith shell, which for J_1 there are six neighbors in the cubic lattice. The fraction

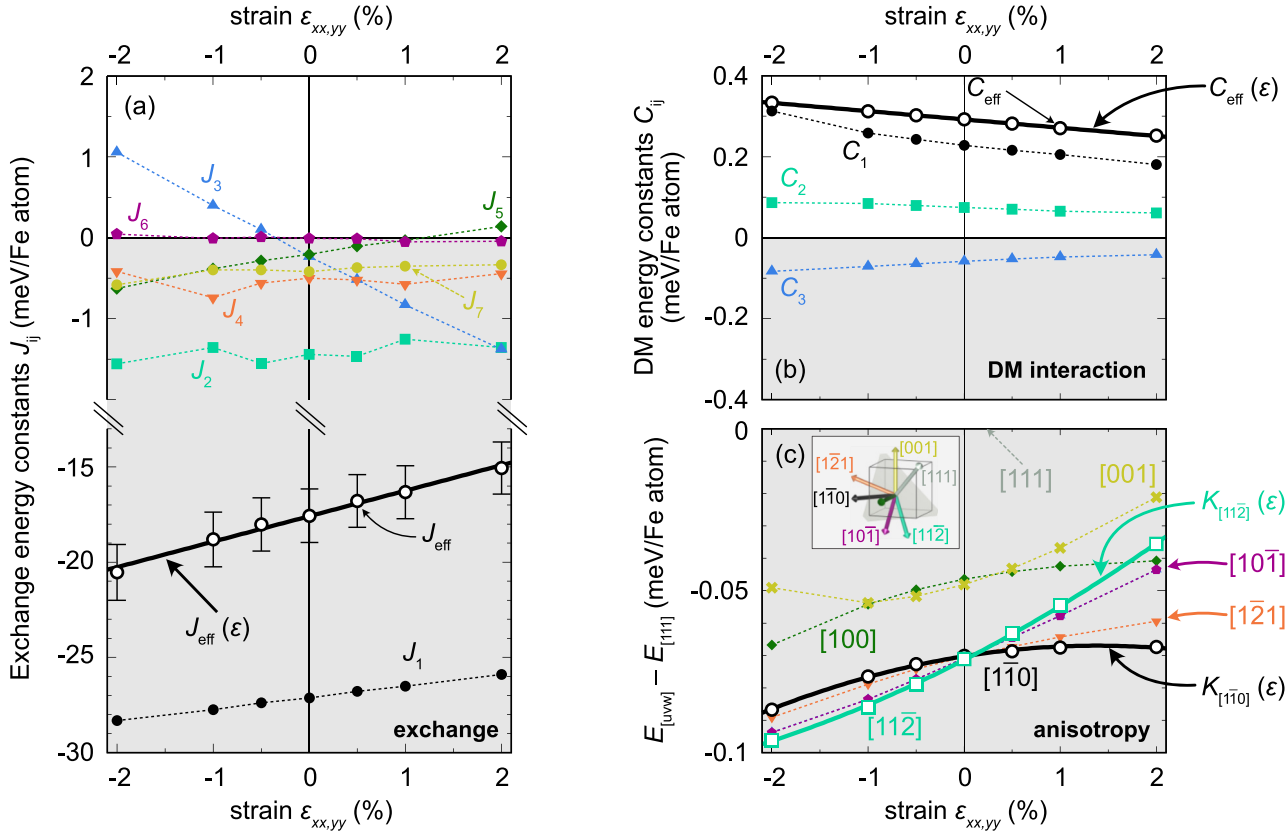

FIG. 2. Trend of magnetic interactions in $BiFeO_3$ under biaxial strain. (a) Magnetic Heisenberg exchange interaction parameters $J_{1...7}$ from pseudocubic approximation for different values of strain. Note that the nearest-neighbor exchange J_1 is dominant and the effective nearest-neighbor exchange J_{eff} matches the curvature of an energy dispersion at $\mathbf{q} \to R$. The error on J_{eff} is stemming from ΔJ_i as described in the text. (b) Evaluated spin-current driven Dzyaloshinskii-Moriya interaction ($C_{1...3}$ for the first three nearest neighbors and in effective nearest-neighbor approximation C_{eff}). (c) Energy differences for uniaxial anisotropy calculations of different magnetization directions with respect to the [111] direction—the inset shows a sketch with all directions in pseudocubic approximation. Note that in the absence of strain, magnetization directions within the (111) plane are energetically degenerate. In all graphs, dashed lines serve as guide to the eye; bold solid lines $J_{eff}(\varepsilon)$, $C_{eff}(\varepsilon)$, and $K_{[uvw]}(\varepsilon)$ are linear fits for J_{eff} and C_{eff} and quadratic fits for the preferred anisotropy directions respectively.

1/6 in front of the square root accounts for the number of the nearest neighbors.

Using multiplication or division, we will use the error estimate according to

$$\Delta Q = |Q| \sqrt{\left(\frac{\Delta J_{eff}}{J_{eff}}\right)^2} = |Q| \frac{\Delta J_{eff}}{J_{eff}} \tag{5}$$

where Q is the quantity we determine.

III. RESULTS

Figure 2 shows the trends of magnetic interactions in $BiFeO_3$ (BFO) under the application of biaxial strain.

A. Exchange interaction

For all applied values of strain, the nearest-neighbor Heisenberg exchange interaction J_1 [black points in Fig. 2(a)] contains the dominant exchange contribution and prefers collinear antiferromagnetic order. Its strength decreases linearly about 10% from -28 meV/Fe atom at $\varepsilon = -2\%$ to -26 meV/Fe atom at $\varepsilon = +2\%$. The second largest contribution stems from the second neighbor $J_2 \approx -1.5$ meV/Fe atom (light green squares). Its strength does not vary drastically with strain, but it leads to exchange frustration with strain as the ratio J_2/J_1 increases. The largest variation can be seen for the third neighbor exchange interaction J_3 [blue triangles in Fig. 2(a)]. For compressive strain, it prefers FM alignment, whereas for tensile strain it prefers AFM alignment. It linearly decreases from $J_3(\varepsilon = -2\%) = 1$ meV/Fe atom to $J_3(\varepsilon = +2\%) = -1$ meV/Fe atom. Neighbors beyond the third shell in the system hold a minor contribution ($|J_{4,5,6,7}|/|J_1| \leqslant 0.03$) and do not change significantly with strain. Even though J_5 undergoes a sign change it only appears as a slight correction in our method.

To simplify the model, we evaluate the effective nearest-neighbor exchange J_{eff} as shown in black circles of Fig. 2(a). It reduces its strength linearly with strain (from ≈ -20 to ≈ -15 meV/Fe atom), with a rate of $\Delta J_{eff}(\varepsilon) = 1.33 \frac{\text{meV/Fe atom}}{\%\text{strain}}$. That means that starting from BFO with no strain, collinear order is preferred by the exchange interaction with compressive strain, whereas it is weakened with tensile strain. This trend is in agreement with Ref. [62], where the authors also find a linear trend in the largest exchange contribution in our range of strain [63].

From Fig. 2(a) it is evident that J_{eff} deviates from J_1. The ratio $\mathcal{F} = J_{\text{eff}}/J_1$ is a good indicator for exchange frustration in magnetic systems [64], where $\mathcal{F} \approx 1$ describes a slightly exchange frustrated system and ratios for $0 < \mathcal{F} << 1$ indicate a strongly frustrated system. For BFO, $\mathcal{F}$ decreases with strain from $\mathcal{F}(\varepsilon = -2\%) = 0.75$ to $\mathcal{F}(\varepsilon = +2\%) = 0.60$. That means that a slight exchange frustration is induced from compressive to tensile strain. Note that for $\mathcal{F} \approx 0.2$ [65] and 0.3 [64], ferromagnetic skyrmions in the absence of magnetic field have been observed and predicted, respectively. These ratios are much smaller than in $BiFeO_3$ and, hence, magnetic skyrmions driven by exchange frustration are not expected to occur in BFO. In order to be stabilized, skyrmions and other topological magnetic structures rely on the interplay of magnetic exchange, DMI, and anisotropy.

B. Dzyaloshinskii-Moriya interaction

We investigate the behavior of the DMI under strain in Fig. 2(b). As we have shown for bulk BFO [46], we have used the converse spin-current model [59,60] to describe our DFT results for the DMI [Eq. (3)]. C_1 (black points) is decreasing almost linearly from compressive to tensile strain, and the variation of C_2 (green squares) and C_3 (blue triangles) is rather small; however, they have opposite signs at almost the same magnitude for each value of strain. Effectively, the DMI (black circles) decreases with strain from $C_{\text{eff}} = 0.33$ meV/Fe atom at $\varepsilon = -2\%$ to $C_{\text{eff}} = 0.25$ meV/Fe atom at $\varepsilon = +2\%$. This is a change rate of about $\Delta C_{\text{eff}}(\varepsilon) = -0.02 \frac{\text{meV/Fe atom}}{\%\text{strain}}$. That means that compared to $R3c$ BFO, the DMI increases with compression preferring noncollinear order and weakens with tensile strain which lowers the energy for noncollinear order. This is opposite to the trend of the exchange interaction, hence it is important to compare their ratios.

C. Magnetocrystalline anisotropy

As third magnetic interaction, we focus on the magnetocrystalline anisotropy [Fig. 2(c)]. We determine the energy of different crystallographic directions with respect to the hard [111] axis. In Ref. [46], we have shown that in $R3c$ bulk BFO, the magnetocrystalline anisotropy energy is lowest and degenerate within the full (111) plane. Here, in the absence of strain ($\varepsilon = 0\%$), we see the same phenomenon: The calculated directions $[1\bar{1}0]$ (black points), $[11\bar{2}]$ (light green squares), $10\bar{1}$ (purple pentagons), and $[1\bar{2}1]$ (orange upside-down triangles) have the same energy at -0.07 meV/Fe atom (note that a tiny deviation is caused by the imposed Cc phase at 0% of strain). The [100] and the [001] directions (dark green rhombus and lighter green x, respectively) are slightly higher in energy.

Applying strain changes this behavior and the energy degeneracy of the different directions is lifted. For tensile strain $\varepsilon > 0$, the $[1\bar{1}0]$ direction is almost constant in energy while the other directions become unfavorable, most of all the $[11\bar{2}]$ direction. For compressive strain, the effect is reversed. The $[1\bar{1}0]$ direction gains the least energy, whereas the $[11\bar{2}]$ direction becomes the preferred magnetization direction by the anisotropy. The value increases from -0.07 meV/Fe atom without strain by 40% to -0.1 meV/Fe atom at $\varepsilon = -2\%$. We focus on the two directions with lowest energies, $[11\bar{2}]$ and $[1\bar{1}0]$. The behavior of their energies with respect to applied strain differs qualitatively from those of the exchange and DMI of Figs. 2(a) and 2(b). Here, we can apply a quadratic fit to describe the trend of the anisotropy with strain $K_{[uvw]}(\varepsilon)$. Following the trend for the two interactions, for larger compressive strains, the $[1\bar{1}0]$ direction will be lower in energy than the $[11\bar{2}]$ direction—in accordance with DFT calculations of Ref. [66] where the authors also find an easy (111) plane for 0% of strain and the $[1\bar{1}0]$ easy axis for large compression. However, in the low strain regime, our results slightly differ.

With respect to the $R3c$ phase of BFO, compression leads to an increased MAE, which favors the collinear order of the G-type AFM state. For tensile strain, the MAE remains similar to that of bulk BFO, so a change of the magnetic ground state is not expected from the MAE. In the following, we will discuss the magnetic ground states we derive from our calculations, compare them to current experimental results, and show which regime of strain could stabilize potential topological magnetic structures.

IV. DISCUSSION

For over a decade, the different magnetic textures in strained $BiFeO_3$ have been intensively investigated in experiments. However, while several studies show a destruction of the cycloidal order with large compressive strain of BFO on $SrTiO_3$ substrates (estimated strain of $-1.5\% < \varepsilon < -0.5\%$ depending on the thickness of BFO) [21,37–40,67,68], others report the persistence of cycloidal order in the same system [69,70]. For tensile strain, the literature is not equivalently vast, but the destruction of the cycloid with large tensile strain has also been observed [21,70]. There, the amount of applied strain to stabilize collinear order differs by $\approx$1%. These results show that the magnetic ground state in strained BFO is very sensitive to the thickness and growth conditions. Different cycloids, such as the type-I and type-II cycloids in $[1\bar{1}0]$ and $[11\bar{2}]$ directions, respectively, as well as the collinear G-type AFM states are extremely close in energy. Hence, small distortions have a large impact on the magnetic ground state. As we will show in the following, this behavior is in agreement with our calculations because different magnetic states are within energy ranges down to 10 μeV/atom.

In general, the magnetic ground state is driven by the interplay between the magnetic exchange J, the DMI C, and the anisotropy K. For example, when K is large as compared to J and C a collinear FM or AFM ground state is favored depending on the sign of J. When C is large, a noncollinear ground state is favored since the DMI favors 90° spin spirals. The ratio between the different contributions is therefore important. We compare these in Fig. 3. In Fig. 3(a), the ratio of $|J_{\text{eff}}|/|C_{\text{eff}}|$ is shown in gray (squares show the ratios of DFT determined magnetic interactions—the bold line is the ratio of the fitted interactions with strain). Increasing the ratios means that collinear order is enhanced, and decreasing ratios destabilize collinear magnetic ground states.

Applying compressive strain, the exchange interaction slightly increases with respect to the DMI—collinear G-type AFM order is more favorable than in the absence of strain.

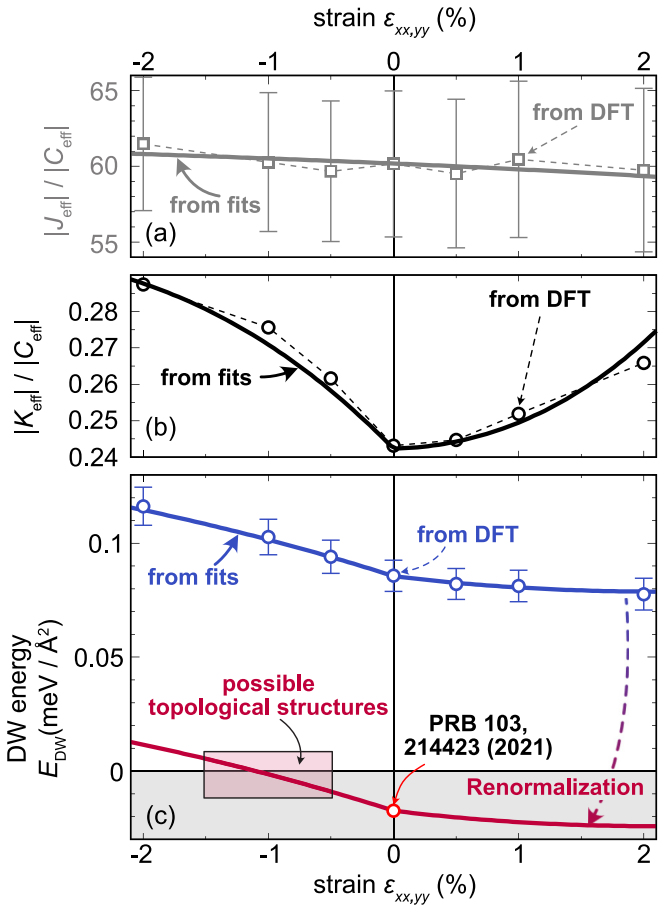

FIG. 3. Interplay between the magnetic interactions for different values of strain. (a) Ratio of magnetic exchange J_{eff} with respect to the Dzyaloshinskii-Moriya interaction C_{eff}. Note that the large error estimate stems solely from the small error ΔJ_{eff}. The squares show the values determined from DFT whereas the solid line shows the ratio $J_{\text{eff}}(\varepsilon)/C_{\text{eff}}(\varepsilon)$ from the fits of Figs. 2(a) and 2(b). (b) Ratio between anisotropy energy K_{eff} and C_{eff}. The circles show the values determined from DFT whereas the solid line shows the ratio $K_{\text{eff}}(\varepsilon)/C_{\text{eff}}(\varepsilon)$ from the fits of Figs. 2(b) and 2(c), where K_{eff} denotes the direction of lowest energy. (c) Domain wall energy E_{DW} [Eq. (6)] as a function of applied strain. The blue points are derived from the DFT values and the blue solid line shows the trend from the fits of $J_{\text{eff}}(\varepsilon)$, $C_{\text{eff}}(\varepsilon)$, and $K_{\text{eff}}(\varepsilon)$. The red point shows the determined value for the $R3c$ phase of BFO according to Ref. [45] where the red line denotes the trend which is renormalized to that point.

With tensile strain, the ratio lowers—hence, noncollinear order gains energy.

The anisotropy [Fig. 3(b)] increases for compressive strain from about 24% to almost 29% of the DMI due to the increasing preference of the $[11\bar{2}]$ direction shown in Fig. 2(c). This enhances the stability of collinear order with a quantization axis along $[11\bar{2}]$. With tensile strain, the preferred magnetization direction changes to $[1\bar{1}0]$ with a constant value of the anisotropy. As the DMI decreases, the ratio K/C increases and will also stabilize collinear magnetic order. Note that the increase of anisotropy with respect to DMI starting from 0% of strain differs for compressive and tensile strain—e.g., a ratio of 0.26 is reached at $\approx +1.5\%$ within the tensile regime, but at around $\approx -0.75\%$ in the compressive regime. Due to both increasing J/C and K/C with compression, we expect collinear order to be favored even in low strain regimes compared to the $R3c$ bulk BFO phase. For tensile strain, the conclusion is not that unambiguous: while the exchange loses energy with respect to the DMI, the anisotropy gains energy. The magnetic behavior crucially depends on both trends. In Fig. 2, the effective exchange and DMI depend linearly on the nominal strain, but the anisotropy can be described with a quadratic behavior.

To quantify where isolated chiral magnetic textures may be stable, we have used the domain wall energy, defined as [71–73]

$$E_{\text{DW}}(\varepsilon) = \frac{4}{a^2(\varepsilon)}\sqrt{J_{\text{eff}}(\varepsilon)\cdot K_{\text{eff}}(\varepsilon)} - \frac{2\pi}{a^2(\varepsilon)}C_{\text{eff}}(\varepsilon), \qquad (6)$$

with $a(\varepsilon)$ being the pseudocubic lattice constant for each value of strain, taken from the diagonal [111] direction to address the changes in the c axis due to relaxation. We also renormalized a into the $[1\bar{1}0]$ direction to account for the known type-I cycloid. As compared to other quantities such as the isolated skyrmion energies or vortex energies, the DW energy is independent of the size of the magnetic textures and therefore does not require the expensive spin dynamics energy minimization in a magnetic supercell of at least 100×100 nm [74]. The DW energy is directly quantifying the energy cost or gain of noncollinear textures based on the effective exchange, the anisotropy, and the DMI. Furthermore, a domain wall can be approximated as half of a cycloid, where for positive values of energy, collinear magnetic order is preferred and for negative values of E_{DW}, a spin spiral ground state is expected [75].

In Fig. 3(c), the DW energy with respect to the applied strain is shown. For all values of strain, the DWs are higher in energy than the collinear state (blue points with error bars); however, the energies are extremely small (below 0.1 meV [76]). As described above, compressing BFO prefers collinear order, i.e., an increased DW energy. For tensile strain, the energy differences are almost zero, meaning that we predict a similar ground state compared to the magnetic state at 0% strain. The trend coincides with experimental observations: For compressive strain, the collinear G-type AFM state is preferred, driven by the large increase of anisotropy in the $[11\bar{2}]$ direction and the increase in exchange with respect to the DMI. This result is robust against small errors within our calculated interactions. For tensile strain, our results show the same difficulties as for experimental observations: The energies of the states are so close that with slightly differing strains the magnetic ground state can differ (see Refs. [21,70]). This is indicated by the error bars from our calculations.

As a reference point in red, we plot the estimated DW energy from Ref. [45], where we investigated the $R3c$ phase of BFO and slightly adapted the DFT parameters to obtain a spin cycloid with a pitch of $\approx$62 nm. With these parameters (corresponding to $C_{\text{eff}} = 0.66$ meV/Fe atom, $K_{\text{eff}} = 0.069$ meV/Fe atom, and $J_{\text{eff}} = -11.78$ meV/Fe atom), the DW energy is slightly negative (-0.017 meV/Å). Following our estimated trend for the magnetic interactions by renormalizing the DW energy from fits (red curve), we can expect a collinear G-type AFM from $\approx -1.5\%$ of compressive strain and a cycloidal ground state for low compressive strains. In

between these regimes, at compressive strain $-1.5 < \varepsilon_{xx,yy} < -0.5\%$, we expect the transition between noncollinear and collinear order for BFO. This is the region where topologically stable magnetic structures could be stabilized in BFO. Depending on the direction of the polarization and the presence of an external electric field, different topological textures may be stabilized in the region (skyrmions, merons, vortices). However, their stabilization mechanisms and their investigation is out of the scope of the present paper.

V. CONCLUSION

We have investigated the evolution of magnetic interactions in $BiFeO_3$ under biaxial strain between $-2 < \varepsilon_{xx,yy} < +2\%$ using first-principles calculations. Going from compressive to tensile strain, both exchange and Dzyaloshinskii-Moriya interaction decrease linearly whereas the uniaxial anisotropy prefers a $[11\bar{2}]$ magnetization direction for the calculated range of compressive strain and a $[1\bar{1}0]$ axis for tensile strain. Comparing the ratios of the three interactions, collinear *G*-type antiferromagnetic order in $BiFeO_3$ is strengthened for compressive strain due to a large increase of anisotropy by about 40% in accordance with experimental observations. For tensile strain our results show a similar magnetic ground state as for bulk BFO, where for a slight change in the ratios, also the collinear ground state can be favored. At the transition between the cycloid and the collinear AFM state for medium compressive strain more complex magnetic structures such as skyrmions or merons might occur, which is why we believe this regime to be interesting for further investigation.

ACKNOWLEDGMENTS

B.D. and S.M. thank Prof. Philippe Ghosez, Louis Bastogne, Dr. Subhadeep Bandyopadhyay, Dr. He Xu, and Prof. Matthieu J. Verstraete for helpful discussions. This work is supported by the National Natural Science Foundation of China under Grant No. 12074277, the startup fund from Soochow University, and Priority Academic Program Development of Jiangsu Higher Education Institutions. S.M., B.D., and L.B. acknowledge DARPA Grant No. HR0011727183-D18AP00010 (TEE Program) and the European Union's Horizon 2020 research and innovation program under Grant No. 964931 (TSAR). L.B. also thanks the ARO for Grant No. W911NF-21-1-0113, the Grant MURI ETHOS W911NF-21-2-0162 from the Army Research Office (ARO), and the Vannevar Bush Faculty Fellowship (VBFF) Grant No. N00014-20-1-2834 from the Department of Defense. Computing time was provided by ARCHER and ARCHER2 based in the United Kingdom at National Supercomputing Service with support from the PRACE aisbl, the Consortium d'Équipements de Calcul Intensif (FRS-FNRS Belgium GA 2.5020.11), and the LUMI CECI/Belgium for awarding this project access to the LUMI supercomputer, owned by the EuroHPC Joint Undertaking, hosted by CSC (Finland) and the LUMI consortium through LUMI CECI/Belgium, ULiege-NANOMAT-SKYRM-1. S.M. is a Postdoctoral Researcher (CR) of the Fonds de la Recherche Scientifique - FNRS (F.R.S.-FNRS no. CR 1.B.324.24F). B.D. is a Research Associate (CQ) of the Fonds de la Recherche Scientifique (F.R.S.–FNRS).

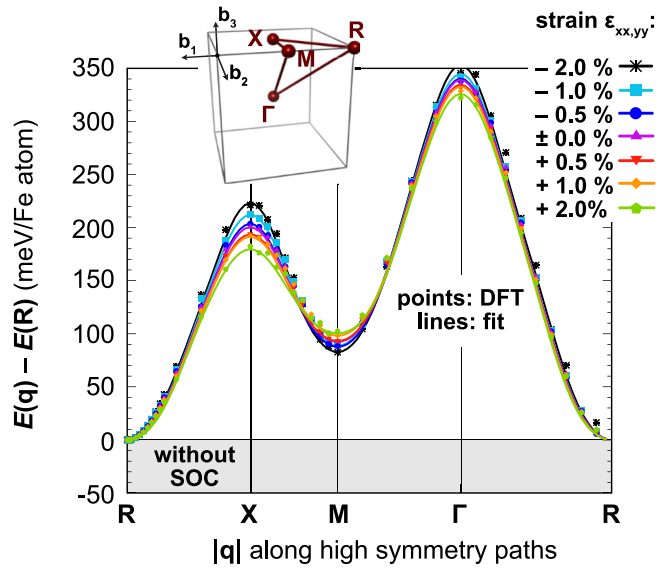

FIG. 4. Energy dispersions $E(\mathbf{q})$ without spin-orbit coupling of homogeneous, flat spin spiral states for Cc $BiFeO_3$ for different amounts of strain with respect to the *G*-type AFM structure energy $E(\mathbf{R})$. Shown are the results along the high-symmetry directions of the pseudocubic first Brillouin zone as shown in the inset. The points are spin spiral energies computed from DFT and the lines are obtained by mapping the Heisenberg exchange Hamiltonian beyond nearest neighbors ($J_{1,\ldots,7}$) to the DFT data. Note that J_{eff} holds the same curvature as $J_{1,\ldots,7}$ at the energy dispersion on the left, where $|\mathbf{q}| \to R$.

APPENDIX: CALCULATED AND FITTED ENERGY DISPERSIONS

As described in the methods section above, we have calculated energy dispersions without and with spin-orbit coupling from DFT to determine the exchange interaction and Dzyaloshinskii-Moriya interaction, respectively. In Fig. 4, the results without SOC are presented. The resulting values for the exchange are shown in Fig. 2(a). The energy contribution due to SOC on the calculated points along the $[1\bar{1}0]$ direction of Fig. 4 are presented in Fig. 5. The results are mapped to

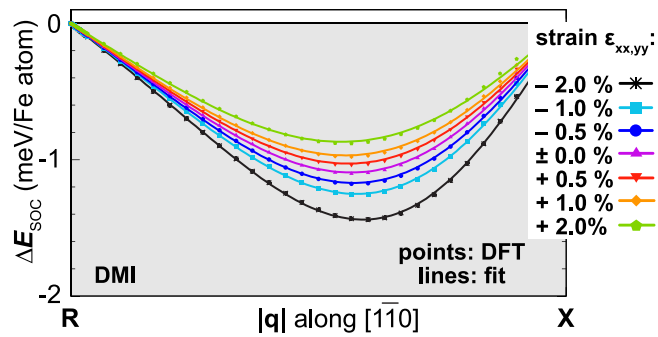

FIG. 5. Energy contribution due to spin-orbit coupling ΔE_{SOC} to the energy dispersion of spin spirals calculated in the $[1\bar{1}0]$ direction of Fig. 4. Shown are the total contributions for each value of strain. The points show the DFT results, whereas the lines represent the fitting of the DMI to determine the contributions $C_{1,2,3}$ of Eq. (3). For C_{eff}, the linear contribution at $|\mathbf{q}| \to R$ is fitted. The error on the fits here is too small to be visible.

Eq. (3) to evaluate the strength of the DMI. The values are displayed in Fig. 2(b), where C_{eff} is the fit at the linear region, $|\mathbf{q}| \to R$. Note that the error on the DMI fit is too small to be visualized in Fig. 2(b).

[1] A. Bogdanov and D. A. Yablonskii, Zh. Eksp. Teor. Fiz. **95**, 178 (1989) [Sov. Phys. JETP **68**, 101 (1989)].

[2] A. Bogdanov and A. Hubert, J. Magn. Magn. Mater. **138**, 255 (1994).

[3] S. Mühlbauer, B. Binz, F. Jonietz, C. Pfleiderer, A. Rosch, A. Neubauer, R. Georgii, and P. Boni, Science **323**, 915 (2009).

[4] X. Z. Yu, Y. Onose, N. Kanazawa, J. H. Park, J. H. Han, Y. Matsui, N. Nagaosa, and Y. Tokura, Nature (London) **465**, 901 (2010).

[5] N. S. Kiselev, A. N. Bogdanov, R. Schäfer, and U. K. Rößler, J. Phys. D **44**, 392001 (2011).

[6] A. Fert, V. Cros, and J. Sampaio, Nat. Nanotechnol. **8**, 152 (2013).

[7] S. Parkin and S.-H. Yang, Nat. Nanotechnol. **10**, 195 (2015).

[8] C. Back, V. Cros, H. Ebert, K. Everschor-Sitte, A. Fert, M. Garst, T. Ma, S. Mankovsky, T. L. Monchesky, M. Mostovoy, N. Nagaosa, S. S. P. Parkin, C. Pfleiderer, N. Reyren, A. Rosch, Y. Taguchi, Y. Tokura, K. von Bergmann, and J. Zang, J. Phys. D **53**, 363001 (2020).

[9] T. Jungwirth, X. Marti, P. Wadley, and J. Wunderlich, Nat. Nanotechnol. **11**, 231 (2016).

[10] X. Zhang, Y. Zhou, and M. Ezawa, Sci. Rep. **6**, 24795 (2016).

[11] J. Barker and O. A. Tretiakov, Phys. Rev. Lett. **116**, 147203 (2016).

[12] T. Jungwirth, J. Sinova, A. Manchon, X. Marti, J. Wunderlich, and C. Felser, Nat. Phys. **14**, 200 (2018).

[13] N. Romming, C. Hanneken, M. Menzel, J. E. Bickel, B. Wolter, K. von Bergmann, A. Kubetzka, and R. Wiesendanger, Science **341**, 636 (2013).

[14] C. Moreau-Luchaire, C. Moutafis, N. Reyren, J. Sampaio, C. A. F. Vaz, N. Van Horne, K. Bouzehouane, K. Garcia, C. Deranlot, P. Warnicke, P. Wohlhüter, J.-M. George, M. Weigand, J. Raabe, V. Cros, and A. Fert, Nat. Nanotechnol. **11**, 444 (2016).

[15] A. Soumyanarayanan, M. Raju, A. L. Gonzalez Oyarce, A. K. C. Tan, M.-Y. Im, A. P. Petrović, P. Ho, K. H. Khoo, M. Tran, C. K. Gan, F. Ernult, and C. Panagopoulos, Nat. Mater. **16**, 898 (2017).

[16] O. Boulle, J. Vogel, H. Yang, S. Pizzini, D. de Souza Chaves, A. Locatelli, T. O. Menteş, A. Sala, L. D. Buda-Prejbeanu, O. Klein, M. Belmeguenai, Y. Roussigné, A. Stashkevich, S. M. Chérif, L. Aballe, M. Foerster, M. Chshiev, S. Auffret, I. M. Miron, and G. Gaudin, Nat. Nanotechnol. **11**, 449 (2016).

[17] M. Hervé, B. Dupé, R. Lopes, M. Böttcher, M. D. Martins, T. Balashov, L. Gerhard, J. Sinova, and W. Wulfhekel, Nat. Commun. **9**, 1015 (2018).

[18] S. D. Pollard, J. A. Garlow, J. Yu, Z. Wang, Y. Zhu, and H. Yang, Nat. Commun. **8**, 14761 (2017).

[19] A. J. Hatt, N. A. Spaldin, and C. Ederer, Phys. Rev. B **81**, 054109 (2010).

[20] B. Dupé, S. Prosandeev, G. Geneste, B. Dkhil, and L. Bellaiche, Phys. Rev. Lett. **106**, 237601 (2011).

[21] D. Sando, A. Agbelele, D. Rahmedov, J. Liu, P. Rovillain, C. Toulouse, I. C. Infante, A. P. Pyatakov, S. Fusil, E. Jacquet, C. Carrétéro, C. Deranlot, S. Lisenkov, D. Wang, J.-M. L. Breton, M. Cazayous, A. Sacuto, J. Juraszek, A. K. Zvezdin, L. Bellaiche *et al.*, Nat. Mater. **12**, 641 (2013).

[22] J. M. Hu, T. Yang, and L. Q. Chen, npj Comput. Mater. **4**, 62 (2018).

[23] J. Wang, Y. Shi, and M. Kamlah, Phys. Rev. B **97**, 024429 (2018).

[24] S. Budhathoki, A. Sapkota, K. M. Law, S. Ranjit, B. Nepal, B. D. Hoskins, A. S. Thind, A. Y. Borisevich, M. E. Jamer, T. J. Anderson, A. D. Koehler, K. D. Hobart, G. M. Stephen, D. Heiman, T. Mewes, R. Mishra, J. C. Gallagher, and A. J. Hauser, Phys. Rev. B **101**, 220405(R) (2020).

[25] Y. Zhang, J. Liu, Y. Dong, S. Wu, J. Zhang, J. Wang, J. Lu, A. Rückriegel, H. Wang, R. Duine, H. Yu, Z. Luo, K. Shen, and J. Zhang, Phys. Rev. Lett. **127**, 117204 (2021).

[26] V. Govinden, P. Tong, X. Guo, Q. Zhang, S. Mantri, M. M. Seyfouri, S. Prokhorenko, Y. Nahas, Y. Wu, L. Bellaiche, T. Sun, H. Tian, Z. Hong, N. Valanoor, and D. Sando, Nat. Commun. **14**, 4178 (2023).

[27] B. W. Qiang, N. Togashi, S. Momose, T. Wada, T. Hajiri, M. Kuwahara, and H. Asano, Appl. Phys. Lett. **117**, 142401 (2020).

[28] P. Hemme, J.-C. Philippe, A. Medeiros, A. Alekhin, S. Houver, Y. Gallais, A. Sacuto, A. Forget, D. Colson, S. Mantri, B. Xu, L. Bellaiche, and M. Cazayous, Phys. Rev. Lett. **131**, 116801 (2023).

[29] P. Dufour, A. Abdelsamie, J. Fischer, A. Finco, A. Haykal, M. F. Sarott, S. Varotto, C. Carrétéro, S. Collin, F. Godel, N. Jaouen, M. Viret, M. Trassin, K. Bouzehouane, V. Jacques, J.-Y. Chauleau, S. Fusil, and V. Garcia, Nano Lett. **23**, 9073 (2023).

[30] Y. E. Roginskaya, Y. Y. Tomashpol'Skiĭ, Y. N. Venevtsev, V. M. Petrov, and G. S. Zhdanov, Sov. Phys. JETP **23**, 47 (1966).

[31] J. B. Neaton, C. Ederer, U. V. Waghmare, N. A. Spaldin, and K. M. Rabe, Phys. Rev. B **71**, 014113 (2005).

[32] P. Ravindran, R. Vidya, A. Kjekshus, H. Fjellvåg, and O. Eriksson, Phys. Rev. B **74**, 224412 (2006).

[33] I. A. Kornev, S. Lisenkov, R. Haumont, B. Dkhil, and L. Bellaiche, Phys. Rev. Lett. **99**, 227602 (2007).

[34] R. Haumont, I. A. Kornev, S. Lisenkov, L. Bellaiche, J. Kreisel, and B. Dkhil, Phys. Rev. B **78**, 134108 (2008).

[35] I. Sosnowska, T. P. Neumaier, and E. Steichele, J. Phys. C **15**, 4835 (1982).

[36] I. Sosnowska, R. Przeniosło, P. Fischer, and V. Murashov, J. Magn. Magn. Mater. **160**, 384 (1996).

[37] F. Bai, J. Wang, M. Wuttig, J. Li, N. Wang, A. P. Pyatakov, A. K. Zvezdin, L. E. Cross, and D. Viehland, Appl. Phys. Lett. **86**, 032511 (2005).

[38] H. Béa, M. Bibes, S. Petit, J. Kreisel, and A. Barthélémy, Philos. Mag. Lett. **87**, 165 (2007).

[39] T. Zhao, A. Scholl, F. Zavaliche, K. Lee, M. Barry, A. Doran, M. P. Cruz, Y. H. Chu, C. Ederer, N. A. Spaldin, R. R. Das, D. M. Kim, S. H. Baek, C. B. Eom, and R. Ramesh, Nat. Mater. **5**, 823 (2006).

[40] W. Ratcliff II, D. Kan, W. Chen, S. Watson, S. Chi, R. Erwin, G. J. McIntyre, S. C. Capelli, and I. Takeuchi, Adv. Funct. Mater. **21**, 1567 (2011).

[41] www.abinit.org.

[42] X. Gonze, B. Amadon, G. Antonius, F. Arnardi, L. Baguet, J.-M. Beuken, J. Bieder, F. Bottin, J. Bouchet, E. Bousquet, N. Brouwer, F. Bruneval, G. Brunin, T. Cavignac, J.-B. Charraud, W. Chen, M. Côté, S. Cottenier, J. Denier, G. Geneste *et al.*, Comput. Phys. Commun. **248**, 107042 (2020).

[43] P. E. Blöchl, Phys. Rev. B **50**, 17953 (1994).

[44] C. Paillard, B. Xu, B. Dkhil, G. Geneste, and L. Bellaiche, Phys. Rev. Lett. **116**, 247401 (2016).

[45] B. Xu, S. Meyer, M. J. Verstraete, L. Bellaiche, and B. Dupé, Phys. Rev. B **103**, 214423 (2021).

[46] S. Meyer, B. Xu, M. J. Verstraete, L. Bellaiche, and B. Dupé, Phys. Rev. B **108**, 024403 (2023).

[47] H. Krakauer, M. Posternak, and A. J. Freeman, Phys. Rev. B **19**, 1706 (1979).

[48] E. Wimmer, H. Krakauer, M. Weinert, and A. J. Freeman, Phys. Rev. B **24**, 864 (1981).

[49] M. Weinert, E. Wimmer, and A. J. Freeman, Phys. Rev. B **26**, 4571 (1982).

[50] www.flapw.de.

[51] S. H. Vosko, L. Wilk, and M. Nusair, Can. J. Phys. **58**, 1200 (1980).

[52] L. M. Sandratskii, J. Phys.: Condens. Matter **3**, 8565 (1991).

[53] A. Mackintosh and O. Andersen, in *Electrons at the Fermi Surface*, edited by M. Springford (Cambridge University, London, 1980), p. 149.

[54] A. Oswald, R. Zeller, P. J. Braspenning, and P. H. Dederichs, J. Phys. F **15**, 193 (1985).

[55] M. Heide, G. Bihlmayer, and S. Blügel, Phys. B: Condens. Matter **404**, 2678 (2009).

[56] S. Meyer, B. Dupé, P. Ferriani, and S. Heinze, Phys. Rev. B **96**, 094408 (2017).

[57] I. Dzyaloshinsky, J. Phys. Chem. Solids **4**, 241 (1958).

[58] T. Moriya, Phys. Rev. **120**, 91 (1960).

[59] H. Katsura, N. Nagaosa, and A. V. Balatsky, Phys. Rev. Lett. **95**, 057205 (2005).

[60] D. Rahmedov, D. Wang, J. Íñiguez, and L. Bellaiche, Phys. Rev. Lett. **109**, 037207 (2012).

[61] Note that we have shown in Ref. [46] that the spin current DMI is mainly driven by the Fe-Bi displacement rather than the oxygen octahedra tilts. The oxygen octahedra are more important for the DMI that is related to the weak ferromagnetic order of the antiferromagnetic (and not cycloidal) state which we do not address within our paper.

[62] M. R. Walden, C. V. Ciobanu, and G. L. Brennecka, J. Appl. Phys. **130**, 104102 (2021).

[63] Note that in Ref. [62], the authors distinguish between in-plane and out-of-plane components of the exchange, whereas we use a pseudocubic approximation.

[64] S. Meyer, Complex spin structures in frustrated ultrathin films, Ph.D. thesis, Christian-Albrechts University of Kiel, 2020, https://nbn-resolving.org/urn:nbn:de:gbv:8-mods-2020-00349-2.

[65] S. Meyer, M. Perini, S. von Malottki, A. Kubetzka, R. Wiesendanger, K. von Bergmann, and S. Heinze, Nat. Commun. **10**, 3823 (2019).

[66] Z. Chen, Z. Chen, C.-Y. Kuo, Y. Tang, L. R. Dedon, Q. Li, L. Zhang, C. Klewe, Y.-L. Huang, B. Prasad, A. Farhan, M. Yang, J. D. Clarkson, S. Das, S. Manipatruni, A. Tanaka, P. Shafer, E. Arenholz, A. Scholl, Y.-H. Chu *et al.*, Nat. Commun. **9**, 3764 (2018).

[67] I. C. Infante, S. Lisenkov, B. Dupé, M. Bibes, S. Fusil, E. Jacquet, G. Geneste, S. Petit, A. Courtial, J. Juraszek, L. Bellaiche, A. Barthélémy, and B. Dkhil, Phys. Rev. Lett. **105**, 057601 (2010).

[68] D. Sando, A. Agbelele, C. Daumont, D. Rahmedov, W. Ren, I. C. Infante, S. Lisenkov, S. Prosandeev, S. Fusil, E. Jacquet, C. Carrétéro, S. Petit, M. Cazayous, J. Juraszek, J.-M. L. Breton, L. Bellaiche, B. Dkhil, A. Barthélémy, and M. Bibes, Phil. Trans. R. Soc. A **372**, 20120438 (2014).

[69] X. Ke, P. P. Zhang, S. H. Baek, J. Zarestky, W. Tian, and C. B. Eom, Phys. Rev. B **82**, 134448 (2010).

[70] A. Haykal, J. Fischer, W. Akhtar, J.-Y. Chauleau, D. Sando, A. Finco, F. Godel, Y. A. Birkhölzer, C. Carrétéro, N. Jaouen, M. Bibes, M. Viret, S. Fusil, V. Jacques, and V. Garcia, Nat. Commun. **11**, 1704 (2020).

[71] D. J. Craik, *Magnetism: Principles and Applications* (Wiley, 1995).

[72] E. D. T. de Lacheisserie, D. Gignoux, and M. Schlenker, *Magnetism* (Springer, New York, 2005), Vol. 1.

[73] S. Rohart and A. Thiaville, Phys. Rev. B **88**, 184422 (2013).

[74] Note that compared to this paper, in Ref. [77], the authors assume a [111] directed anisotropy which exceeds the bulk value by a factor of 3 to stabilize magnetic Skyrmions in BFO. Here, we have calculated the anisotropy based on DFT and only find an easy axis within the (111) plane.

[75] Note that contrary to the spin spiral pitch λ, the DW width $\Delta \propto \sqrt{J/K}$ is independent of the DMI, hence for spin spirals with a certain pitch length the quantitative description differs as well as its energy. However, due to the simplicity of Eq. (6), the trends for the magnetic ground-state energies can be recognized directly and give qualitatively the same results as spin spiral energies.

[76] Note that we expect a small energy offset due to systematic errors coming from the DFT (the functional, the Hubbard correction, the geometry, etc.). The offset on the energies is impossible to quantify, but should be consistent throughout all our calculations.

[77] Z. Li, T. Chirac, J. Tranchida, V. Garcia, S. Fusil, V. Jacques, J.-Y. Chauleau, and M. Viret, Phys. Rev. Res. **5**, 043109 (2023).